# Topological wave phenomena in photonic time quasicrystals

Xiang Ni,[1,2] Shixiong Yin,[2,3] Huanan Li,[2,4] and Andrea Alù[2,3,5]

[1]*School of Physics, Central South University, Changsha 410083, China*

[2]*Photonics Initiative, Advanced Science Research Center, City University of New York, New York, New York 10031, USA*

[3]*Department of Electrical Engineering, City College of The City University of New York, New York 10031, USA*

[4]*MOE Key Laboratory of Weak-Light Nonlinear Photonics, School of Physics, Nankai University, Tianjin 300071, China*

[5]*Physics Program, Graduate Center, City University of New York, New York, New York 10016, USA*

(Received 17 February 2024; revised 18 February 2025; accepted 24 February 2025; published 27 March 2025)

Time interfaces consist of abrupt and spatially uniform changes in the optical properties of a medium. Their periodic occurrence forms photonic time crystals, which offer opportunities to tailor classical and quantum light-matter interactions. Here we explore one-dimensional photonic time quasicrystals, formed when time interfaces occur in a quasiperiodic fashion featuring long-range order. We unveil the emergence of topological phases and Hofstadter butterfly spectra in these systems, and demonstrate that their temporal response emulates the localization of topological edge states, enabling the temporal analog of topological Thouless pumping. Our findings open avenues for topological photonics leveraging time as a synthetic dimension, with functionalities that go beyond their spatial counterparts.

DOI: 10.1103/PhysRevB.111.125421

## I. INTRODUCTION

Photonic time-interfaces, obtained by abruptly changing the optical properties of a medium homogenously in space, have been explored for the past few decades [1–3] for wave control; yet only recently the experimental observation of temporal reflections at a time interface has been reported for electromagnetic waves [4]. Since time is bound to flow towards the future, time-reflected signals exist in the same medium as time-transmitted waves, but they propagate in opposite directions [5]. Another difference between temporal and spatial reflections is given by the governing conservation laws. Since temporal switching preserves spatial translational symmetry but not time translational symmetry, the wave momentum is conserved, while their energy and frequency are not. These features, along with the associated temporal degrees of freedom, have been exploited to enable inverse prism phenomena [6], broadband amplification and absorption [7,8], temporal aiming [9], unitary energy transfer [10] and extreme energy transformations [11] and temporal Faraday rotation [12]. Other exciting opportunities are unveiled by combining multiple time interfaces: when occurring in a periodic fashion time interfaces form photonic time crystals (PTCs)—the temporal dual of spatial photonic crystals [13–16]. Since energy is not conserved at time interfaces, PTCs support momentum bandgaps that amplify temporally evanescent waves. These phenomena open interesting opportunities for fundamental science and applications, such as quantum sensors, enhanced Purcell effects, and quantum amplified emission [17–22].

In a different context, topological photonics has enabled in recent years exotic optical phenomena [23–25], such as robust edge modes immune from backscattering, with opportunities for classical and quantum applications [26–36]. Photonic quasicrystals, aperiodic structures with long-range spatial order, also support interesting topological features, such as Hofstadter butterfly patterns, topological Thouless pumping, and topological order attributed to higher dimensions [37–43]. Building on the duality between spatial and temporal interfaces, topological phenomena in PTCs have recently started to emerge. Recent works have unveiled topological aspects of photonic/phononic time crystals in homogeneous time-switched media emulating the Su-Schrieffer-Heeger model in the time domain [44,45], and disordered PTCs supporting the temporal analog of Anderson localization [46,47].

Despite these advances in PTCs, photonic time quasicrystals (PTQCs), formed by nonperiodic sequences of time interfaces that retain long-range order, have remained so far elusive. Spatial photonic quasicrystals possess a fractal spectrum and support interesting topological wave phenomena, hence it is interesting to explore whether these features may arise in PTQCs. For example, in analogy with topological photonics is it possible to define a topological invariant for PTQCs, and introduce a temporal cladding slab (TCS) forming a temporal interface with PTQCs at which topological edge states emerge? How do we even measure the spectra of temporal edge states and interpret their dynamic evolution given the distinct causality constraints that emerge in the time domain? In this work, we endeavor to resolve these questions by investigating the topological features of a temporal structure with a finite number of time slabs approximating a PTQC. By developing an *ad hoc* temporal eigenvalue equation, we unveil the emergence of a Hofstadter butterfly spectrum of such temporal structure, define a topological invariant in synthetic space, and observe topological edge states localized at temporal boundaries. Moreover, we establish a closed-form relation between scattering coefficients and the quasifrequency of the temporal structure's eigenmodes and, based on this result, we explore the temporal dispersion of the topological edge states by recording the transmission at the interfaces of various temporal slabs, which support the temporal analog of topological Thouless pumping in synthetic

 

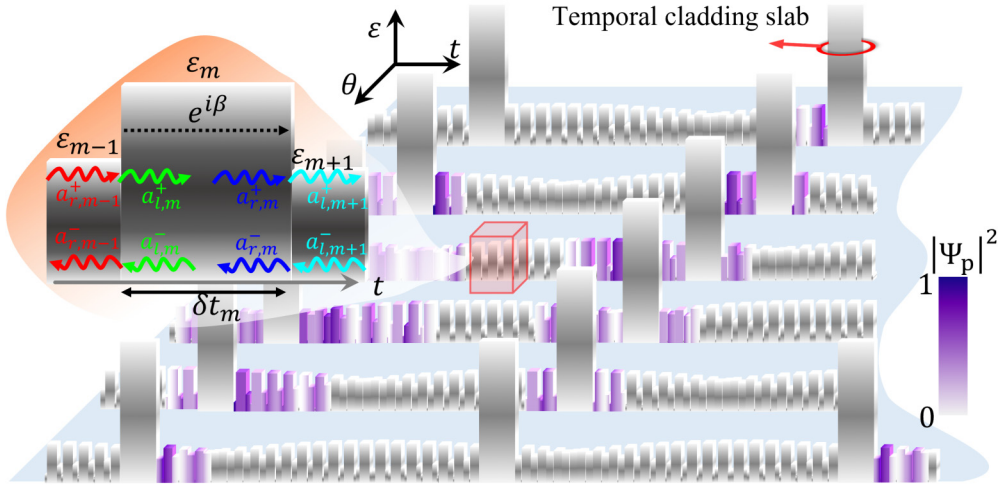


FIG. 1. A photonic time quasicrystal (PTQC) obtained by switching the permittivity $\varepsilon_m$ with time steps $\delta t_m$ and phason parameter $\theta$. Temporal cladding slabs with large permittivity $\varepsilon_{tcs}$ are added after a PTQC sequence (not to scale). The color of the pillars represents the magnitude of the wave functions $|\Psi_p|^2$ evolving with $\theta$. The inset shows forward and backward waves in each PTQC section. The propagation phase $\beta$ is chosen to be equal in each section.

space. We further explore the long-time evolution of waves in our structure and reveal their distinct behavior with and without introducing temporal interfaces through a TCS.

## II. TEMPORAL EIGENVALUE PROBLEM

Consider an electromagnetic field consisting of two counterpropagating waves in an isotropic lossless medium with relative permittivity $\varepsilon$: $E_x(z,t) = e^{-i(k_z z-\omega t)}a^+ + e^{-i(k_z z+\omega t)}a^- + \text{c.c.}; \eta_0 H_y(z,t) = \sqrt{\varepsilon}(e^{-i(k_z z-\omega t)}a^+ - e^{-i(k_z z+\omega t)}a^-) + \text{c.c.}$, where the angular frequency $\omega = k_z c_0/\sqrt{\varepsilon}$, $a^\pm$ are the complex wave amplitudes, $c_0 = \frac{1}{\sqrt{\mu_0\epsilon_0}}$ and $\eta_0 = \sqrt{\mu_0/\epsilon_0}$ are the speed of light and characteristic impedance in free space, respectively. PTQCs are formed by abruptly switching $\varepsilon(t)$ in time uniformly across the medium, and $\varepsilon(t)$ can be periodic such that $\varepsilon(t+T_\text{d}) = \varepsilon(t)(T_\text{d} \to \infty)$ and follows a series of step functions $\varepsilon_m$ (heights of pillars in Fig. 1),

$$\varepsilon(t) = \varepsilon_m = \varepsilon_{m+q}, \quad \text{when } t \neq [t_m,\ t_m + \delta t_m] \bmod T_\text{d}, \quad (1)$$

where $q$ is the total number of switching times within one period, $m = 1,\ 2,\ \ldots,\ q$ are the indices of the time slabs, and $t_m = \sum_{m'=1}^{m-1} \delta t_{m'}$, $m \geqslant 2$, $t_1 = 0$ with $T_\text{d} \equiv t_q + \delta t_q$ being the overall periodicity of the modulation, and $\delta t_m$ (pillar widths in Fig. 1) is the duration of each time slab. The step functions $\varepsilon_m$ are varied according to the sinusoidal function

$$\varepsilon_m = \varepsilon_a + \delta\varepsilon \sin(2\pi m\bar{\alpha} + \theta), \quad (2)$$

where $\varepsilon_a$ is the average permittivity across PTQCs, $\theta \in [0, 2\pi)$ is called phason. The irrational number $\alpha$ can be approximated by the rational number $\bar{\alpha} = \lfloor \alpha \cdot q \rfloor / q$, where $q$ and $p = \lfloor \alpha \cdot q \rfloor$ are integer numbers, thus the temporal structure becomes periodic in time. Since the aperiodicity of the exact PTQC is approached in the limit of a large "temporal supercell", we choose $q$ to be large enough such that the eigenspectrum of the periodic structure can include the fractal features in the eigenspectrum of the quasicrystal up to small corrections. If $q \to \infty$, the model resumes its "quasicrystal" variation in time. As sketched in Fig. 1, we choose a nonuniform time step $\delta t_m$

$$\delta t_m = \delta t_0 \sqrt{\frac{\varepsilon_m}{\varepsilon_a}}, \quad (3)$$

where $\delta t_0$ is the average time step. This choice ensures that the propagation phase $\beta = \omega_m \delta t_m = \frac{ck_z \delta t_m}{\sqrt{\varepsilon_m}} = \frac{ck_z \delta t_0}{\sqrt{\varepsilon_a}}$ accumulated in each time slab is independent of the index $m$, and thus $\beta$ has a constant value. After imposing the continuity of the displacement field $D_x = \varepsilon E_x$ and magnetic field $H_y$ at each time interface and applying the Floquet's theorem, we obtain the temporal eigenvalue equation [48]

$$M_{1\to q}(\beta)\psi(0^+) = e^{-i\varphi}\psi(0^+), \quad (4)$$

where $M_{1\to q}(\beta)$ is the temporal transfer matrix of our structure, $\varphi = \Omega T_\text{d} \in [0, 2\pi)$ is the Floquet phase, and $\Omega$ is the quasifrequency. $\psi(0^+) = [a^+_{l,1}, a^-_{l,1}]^\text{T}$, is composed of the coefficients for forward waves (with positive frequency) and backward waves (with negative frequency) at initial time $t = 0^+$ corresponding to the left boundary of the initial time slab. Equation (4) represents the conventional eigenvalue equations of PTCs, relating the propagation phase $\beta$ to the Floquet phase $\varphi$. However, the topological properties of our temporal structure approximating the PTQC exist in a momentum bandgap and lies in the space $(\varphi, \theta)$. To obtain the fractal spectrum and topological invariants of our temporal supercell, all eigenvalue solutions and scattering coefficients at various time slabs in the space $(\varphi, \theta)$ need to be obtained. As a result, it is neither convenient nor efficient to study the topological properties of it via Eq. (4) which seeks solutions in the space $(\beta, \theta)$.

Therefore, it is highly desirable to develop an alternative eigenvalue approach for large temporal systems in which the roles of momentum and frequency are reversed compared to Eq. (4). Herein, we aim to derive a frequency-momentum eigenvalue equation, exploiting the condition that the phase $\beta$ is conserved at each time slab. As the inset of Fig. 1 shows,

forward and backward waves before and after the temporal interface between time slabs $m$ and $m+1$ are connected by the matching matrix as

$$\begin{pmatrix} a^{+}_{l,m+1} \\ a^{-}_{l,m+1} \end{pmatrix} = \begin{pmatrix} \tau_{m,m+1} & \rho_{m,m+1} \\ \rho_{m,m+1} & \tau_{m,m+1} \end{pmatrix} \begin{pmatrix} a^{+}_{r,m} \\ a^{-}_{r,m} \end{pmatrix}, \tag{5}$$

where $a^{\pm}_{l(r),m}$ are the magnitudes of forward and backward waves at the left(right) boundary of time slab $m$ (refer to the inset of Fig. 1). The relations between waves are rearranged into

$$S_m \begin{pmatrix} a^{+}_{r,m} \\ a^{-}_{l,m+1} \end{pmatrix} = \begin{pmatrix} a^{-}_{r,m} \\ a^{+}_{l,m+1} \end{pmatrix}, \tag{6}$$

where $S_m$ is referred to as the scattering matrix,

$$S_m = \begin{bmatrix} -\rho_{m,m+1} & 1 \\ -\tau_{m,m+1} & 0 \end{bmatrix}^{-1} \begin{bmatrix} \tau_{m,m+1} & 0 \\ \rho_{m,m+1} & -1 \end{bmatrix}, \; m = 1, 2, \ldots, q. \tag{7}$$

The constant phase $\beta$ allows us to rewrite the propagation matrix for each time slab as follows:

$$\begin{pmatrix} a^{+}_{l,m} \\ a^{-}_{r,m} \end{pmatrix} = e^{-i\beta}\sigma_1 \begin{pmatrix} a^{-}_{l,m} \\ a^{+}_{r,m} \end{pmatrix}, \tag{8}$$

where $\sigma_1 = \left[\begin{smallmatrix} 0 & 1 \\ 1 & 0 \end{smallmatrix}\right]$. Combining Eqs. (6) and (8) and Floquet boundary condition $\psi(T_d^{+}) = e^{-i\varphi}\psi(0^{+})$, we obtain compacted linear equations

$$\begin{bmatrix} S_1 & & & \\ & S_2 & & \\ & & \ddots & \\ & & & S_q \end{bmatrix} |u_n\rangle = e^{-i\beta} \begin{bmatrix} & & & e^{i\varphi} \\ & \sigma_1 & & \\ & & \ddots & \\ e^{-i\varphi} & & & \sigma_1 \end{bmatrix} |u_n\rangle, \tag{9}$$

where eigenstates $|u_n(\varphi,\theta)\rangle = [a^{+}_{r,1}, a^{-}_{l,2}, a^{+}_{r,2}, a^{-}_{l,3}, \ldots, a^{+}_{r,q}, a^{-}_{l,q+1}]$ consist of forward waves at the end times and backward waves at the initial times of various time slabs. The Floquet phase factors $e^{\pm i\varphi}$ appear in the off-diagonal matrix stemming from Floquet boundary conditions at the initial and end sites. We define operator $U$ as

$$U = \begin{bmatrix} & & & e^{i\varphi} \\ & \sigma_1 & & \\ & & \ddots & \\ e^{-i\varphi} & & & \sigma_1 \end{bmatrix}^{-1} \begin{bmatrix} S_1 & & & \\ & S_2 & & \\ & & \ddots & \\ & & & S_q \end{bmatrix}. \tag{10}$$

Thus, we treat $\varphi$ as the input variable and evaluate $\beta$ by reformulating Eq. (4) into $2q \times 2q$ closed-form matrix expression

$$U(\varphi,\theta)|u_n(\varphi,\theta)\rangle = e^{-i\beta_n}|u_n(\varphi,\theta)\rangle, \tag{11}$$

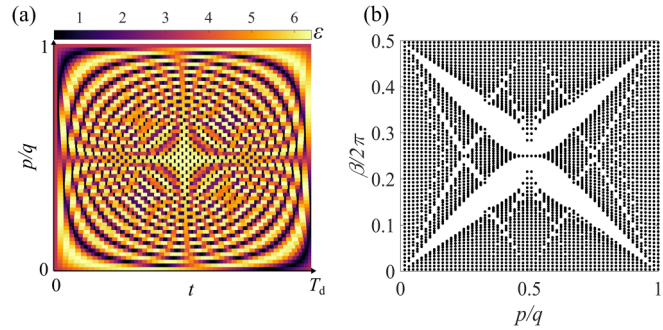


FIG. 2. Hofstadter butterfly spectrum in our temporal supercells. (a) Variation of permittivity in the time domain for different configurations of temporal supercells controlled by $\alpha = p/q$. (b) Hofstadter butterfly eigenvalue spectrum obtained from Eq. (11) with Floquet phase set as $\varphi = \pi/2$. Other parameters are taken as $\theta = 0$, $q = 61$, $p = 0, 1, \ldots, q-1$. $\varepsilon_a = 3.4$, $\delta\varepsilon = 3$. These parameters are the same throughout the manuscript otherwise specified.

where $U(\varphi,\theta)$ is unitary and represents the evolution operator of waves in a single time slab, and $n = 1, 2, \ldots, 2q$ indicate the eigenstate indices according to their phase $\beta_n(\varphi,\theta)$. The eigenvalue Eq. (11) provides an ideal approach to define and evaluate a topological invariant, since its eigenstates $|u_n(\varphi,\theta)\rangle$ are expressed in the space $(\varphi,\theta)$.

## III. HOFSTADTER BUTTERFLY SPECTRUM

The implementation of Aubry-Andrè model with one-dimensional (1D) quasiperiodic platforms opens new ways to study the associated topological phenomena, like the emergence of a fractal energy spectrum encoding self-similarities, and topological pumping [52,53]. Having defined the topological features of our temporal supercell, we may expect distinct features and advantages in this domain over the spatial counterpart. For example, PTQCs avoid complex fabrication requirements of aperiodic structure and enables swift reconfiguration of various topological models on the same platform. In this section, we study whether the essential features of 1D quasiperiodic crystals in the spatial domain can be similarly exhibited in PTQCs. We first explore a model of temporal supercell realized by temporally varying the permittivity of the spatially homogeneous medium according to Eqs. (1)–(3). $\alpha = \frac{p}{q}$ varies from 0 to 1, which controls the varying patterns of permittivity in time and the temporal periods of our temporal supercell, as shown by the schematic in Fig. 2(a). To resolve the fractal structure of the butterfly spectrum and approximating the properties of PTQCs more accurately, the degrees of freedom of our temporal supercell represented by the parameter $q$ needs to be large. Here, we take a specific value $q = 61$ which provides sufficient resolution to observe the major fractal features in the eigenvalue spectrum. To visualize the eigenvalue spectrum and judge whether temporal supercell supports Hofstadter butterfly spectrum, we sweep the parameter $p$ from 0 to $q-1$ and collect all eigenvalues of temporal supercell via Eq. (11) as a function of $p$ in the same plot, see Fig. 2(b). The numerical spectrum reveals the fractal features like the recurrent appearance of the temporal bandgaps, signifying the implicit connection between our

model and the Aubry-Andrè model [48]. Note the spectrum exhibits a period of $\beta_0 = \pi$ since in the modulation scheme $q$ is odd and $\varphi = \pi/2$ which guarantees a period of $\beta_0 = \pi$ [48].

## IV. TEMPORAL TOPOLOGICAL PUMPING

In this section, we explore whether PTQCs can support topological edge states at their temporal boundaries and emulate adiabatic pumping in synthetic dimension. To this end, we consider a temporal supercell in which the permittivity step functions are described by Eq. (2) with fixed $\bar{\alpha} = \frac{p}{q}$ satisfying the rationality condition and with $\theta$, a phason acting as a variable in synthetic Brillouin zone, varying between 0 and $2\pi$. The eigenstates entailed by the effective Hamiltonian can be defined as

$$H_{\text{eff}}(\varphi,\theta)|u_n(\varphi,\theta)\rangle = \beta_n(\varphi,\theta)|u_n(\varphi,\theta)\rangle, \tag{12}$$

where $H_{\text{eff}}(\varphi,\theta) = \frac{i}{T_{\text{d}}}\log[U(\varphi,\theta)]$. The Brillouin zone in the phase variables $(\varphi,\theta)$ forms an $S^1 \times S^1$ torus, which supports a Chern number $c_n = \frac{i}{2\pi}\iint_{\text{BZ}} dSF_n(\varphi,\theta)$ for the $n^{\text{th}}$ temporal band, where the Berry curvature is expressed as $F_n(\varphi,\theta) = \nabla \times \langle u_n(\varphi,\theta)|\nabla u_n(\varphi,\theta)\rangle$. Thus, the Chern number of the $i^{\text{th}}$ temporal bandgap can be evaluated as $C_i = \sum_{n=1}^{N_i} c_n$, where $N_i$ is the number of bands below the temporal bandgap. Interestingly, the two main bandgaps in our temporal supercell have integer quantized Chern number $\pm 1$. For spatial quasicrystals, localized topological edge states are expected to emerge at any boundary, according to the bulk-edge correspondence. To test whether the bulk-edge correspondence also applies to our temporal structure, we introduce spatially homogenous slabs with large permittivity $\varepsilon_{\text{clad}} \gg \varepsilon_m$, playing the role of TCSs, right after the periodic structure sequence by switching the permittivity from $\varepsilon_q$ to $\varepsilon_{\text{clad}}$ after $T_{\text{tqc}}$, i.e., analogous to a spatial trivial medium surrounding a topological photonic crystal. To preserve phase conservation, the time step for TCSs is chosen to be $T_{\text{tcs}} = \delta t_0\sqrt{\varepsilon_{\text{clad}}/\varepsilon_a}$, thus the total period of our temporal structure becomes $T_{\text{d}}' = T_{\text{tqc}} + T_{\text{tcs}}$. We vary the phason $\theta$ cycling from 0 to $2\pi$, and the corresponding variation of permittivity as a function of $\theta$ in the time domain is shown in Fig. 3(a). We then calculate the band structure of temporal structure using Eq. (11) without TCS and with TCS, as shown in Figs. 3(b) and 3(c). Since phase $\varphi$ does not change the topological properties of our temporal structure, without loss of genericity, we choose $\varphi = \pi/2$ in the eigenvalue calculation. Gapless edge bands are absent in momentum bandgaps of temporal bands in Fig. 3(b) while emerge in those of Fig. 3(c), as shown by the orange and blue colored curves, confirming the bulk-edge correspondence works in our temporal structure. To demonstrate topological pumping of temporal edge states, $\theta$ is adiabatically changed and the variation of the eigenstates is plotted over the time domain (denoted by $|\Psi_{\text{p}}|^2$) following the curve indicated by arrows in Fig. 3(c). As shown in Fig. 3(d), the wave is localized at the left temporal boundary when $\theta$ is small. As $\theta$ increases, the edge state merges with bulk states, and then the distribution of wave function shifts to the other temporal boundary. The evolution of edge states tuned by the phason $\theta$ clearly emulates the temporal analogue of adiabatic topological pumping.

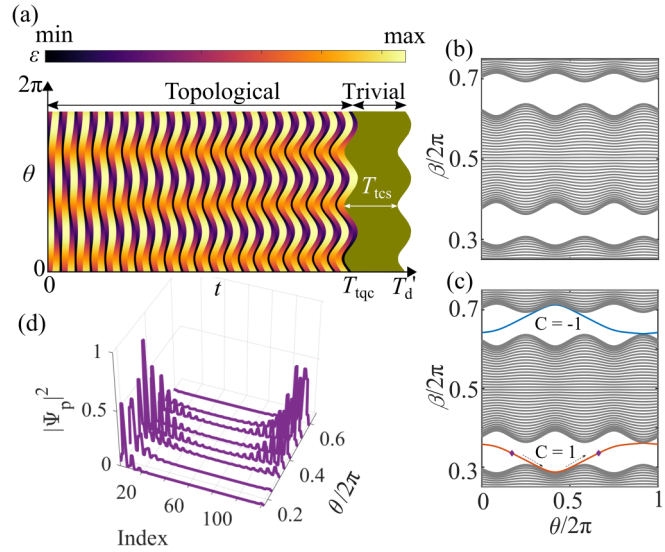


FIG. 3. Adiabatic topological pumping in our temporal structures. (a) Temporal variation of permittivity representing a temporal structure with a temporal cladding slab (TCS) formed by a trivial homogenous slab as a function of $\theta$. The TCS has a width with time step $T_{\text{tcs}} = \delta t_0\sqrt{\varepsilon_{\text{clad}}/\varepsilon_a}$ to preserve the phase $\beta$. Other parameters are $p = 20, q = 60$. (b), (c) Temporal bandstructures of (b) temporal supercells, (c) temporal structures containing TCS. Chern numbers for the two bandgaps are given. (d) Evolution of wave function profiles $|\Psi_{\text{p}}|^2$ calculated with Eq. (11) as a function of $\theta$. The indices are components of the eigenstates representing their field distributions in time. The permittivity for TCS is $\varepsilon_{\text{clad}} = 100$, which is the same throughout the manuscript otherwise specified.

## V. TEMPORAL EDGE BANDS

So far, we have unveiled the topological features of our temporal structure using the eigenvalue Eq. (11). In a practical setup, the scattering coefficients disclose the temporal structure's topological features. Hence, it is important to study the dynamics of excited waves in our temporal structure by collecting their scattering coefficients under the proposed driving protocol. Due to causality, the wave cannot be influenced by the TCS until the TCS is applied. Therefore, the dynamics of the excited waves during the first driving period ($t < T_{\text{d}}'$) cannot be expected to produce temporal edge states. Instead, if we record the real component of the transmission rate $\mathcal{R}e(\gamma)$ obtained after the first period ($t > T_{\text{d}}'$) and right before the permittivity is switched to $\varepsilon_2$ ($t < T_{\text{d}}' + \delta t_1$), the waves will experience a complete period of our temporal structure. The transmission rate can be inferred from transfer matrix $\gamma = M_{11} = M_{22}^*$, where $M_{ij}$ are the elements of $M_{1\to q}$. Due to temporal reciprocity [11], $\mathcal{R}e(\gamma)$ and the corresponding Floquet phase $\varphi$ satisfies the relation [48]

$$\mathcal{R}e(\gamma(\beta_{\text{eig}})) = \cos(\varphi), \tag{13}$$

Therefore, we can tell that eigenmodes are excited when $|\mathcal{R}e(\gamma(\beta))| \leqslant 1$, and determine the phase $\varphi$ from Eq. (13). If the parameters of the launched waves are selected such that eigenmodes are not supported, $|\mathcal{R}e(\gamma(\beta))| > 1$, and Eq. (13) no longer holds. To verify these predictions, we simulate the model described by Eqs. (1)–(3) with $p = 3, q = 9$, and

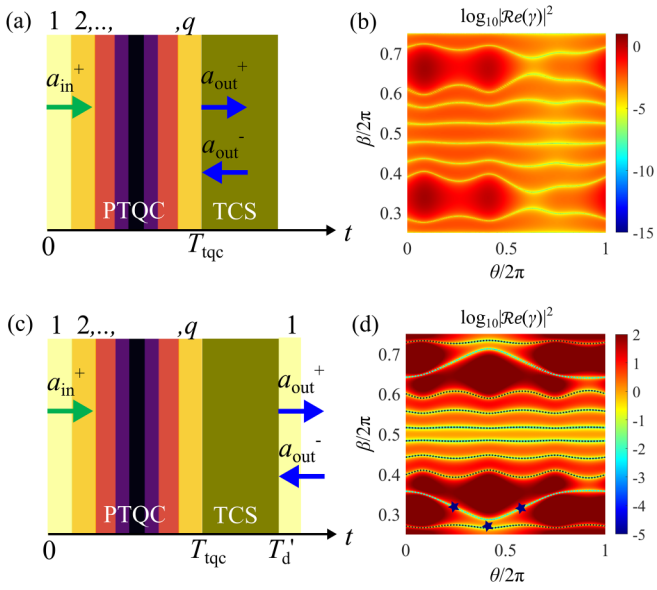


FIG. 4. Temporal edge bands in our temporal structures. (a) Schematic of collecting scattering parameters at the TCS after a period of supercell $T_{tqc}$ and (b) the corresponding spectrum whose value $\log_{10}|\mathcal{R}e(\gamma)|^2$ is encoded in the color of the spectrum as a function of $\theta$ and $\beta$. (c) Schematic of collecting scattering parameters in the initial time slab of our temporal structure after a full period of temporal supercell and TCS $T_d'$ and (d) corresponding spectrum $\log_{10}|\mathcal{R}e(\gamma)|^2$ as a function of $\theta$ and $\beta$. Here $p = 3$, $q = 9$. The value $\log_{10}|\mathcal{R}e(\gamma)|^2$ is produced from the recursive relation in Eq. (4) [or Eq. (S1)] and the band structures shown by black dotted lines are obtained from the eigenvalue Eq. (11).

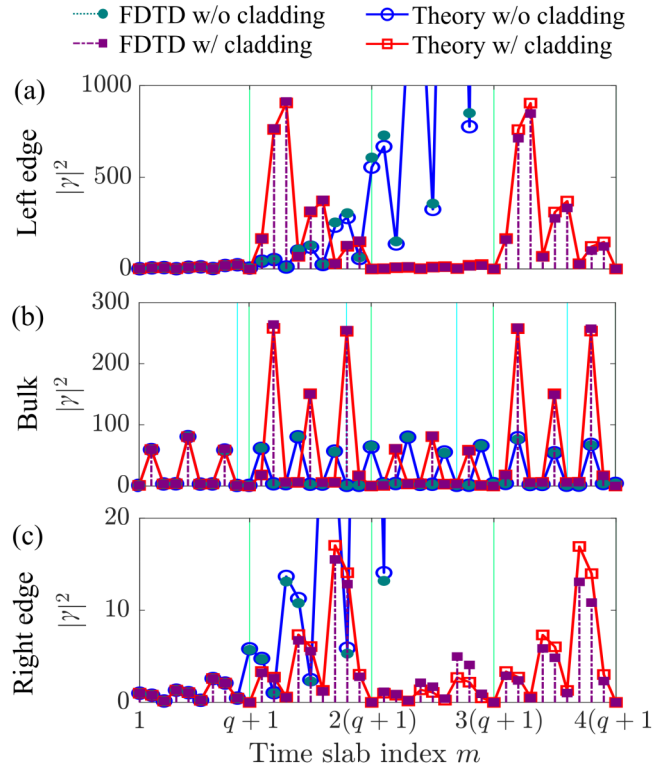


FIG. 5. Temporal evolution of edge modes in our temporal structure across multiple periods. (a) Evolution of edge modes localized at the left temporal interface. (b) Evolution of bulk modes in the temporal structure. (c) Evolution of edge modes localized at the right temporal interface. Parameters normalized to $2\pi$ are adopted for these examples as (a) $(\theta_l, \beta_l) = (0.2412, 0.3189)$, (b) $(\theta_b, \beta_b) = (0.4221, 0.2661)$ and (c) $(\theta_r, \beta_r) = (0.593, 0.3191)$, and their positions are denoted by blue stars in Fig. 4(d). The other parameters are the same as in Fig. 4.

$\theta \in [0, 2\pi)$, which capture the same topological features as the model in Fig. 3, but with a shorter period to facilitate full-wave simulations. We select a forward wave $\psi_i = (1, 0)^T$ in the medium at $t = 0$ as the initial wave, then we evaluate the scattering coefficients associated with the complex temporal transmitted and reflected waves via the recursive relation in Eq. (4) at the temporal boundaries from temporal supercell to TCS and from TCS back to temporal supercell, respectively.

If we record $\mathcal{R}e(\gamma)$ during the time interval between $T_{tqc}$ and $T_d'$, as shown in Fig. 4(a), the spectrum whose color encodes the variation of $\log_{10}|\mathcal{R}e(\gamma)|^2$ as a function of parameters $(\theta, \beta)$ reveals bulk modes [Fig. 4(b)], but no gapless edge mode can be observed in the momentum bandgap. In the second scenario [Fig. 4(c)], we study the scattering coefficients at the time interval between $T_d'$ and $T_d' + \delta t_1$. The spectrum, shown in Fig. 4(d), now reveals the emergence of topological edge modes crossing the momentum bandgaps, and the minima of $|\mathcal{R}e(\gamma)|$ are precisely the bands obtained by Eq. (11) computed for $\varphi = \pi/2$ and indicated by black dots in Fig. 4(d). According to Eq. (13), the minima in spectra of Figs. 4(b) and 4(d) correspond to the eigenvalues computed for both cases and demonstrate similar temporal bulk bands, as expected, but only the latter reveals temporal edge modes crossing the momentum bandgap. To further confirm these results, we perform homemade finite-difference-time-domain (FDTD) simulations for this system. By sweeping the parameter $\theta$ and evaluating $\mathcal{R}e(\gamma) = |\gamma|\cos(\phi_\gamma)$ for each temporal configuration, where $\phi_\gamma$ is the phase of the transmission rate [48], we obtain the spectra $\log_{10}|\mathcal{R}e(\gamma)|^2$ as a function of $(\theta, \beta)$ measured right after $T_{tqc}$ [Fig. S2(c)] and measured right after $T_d'$ [Fig. S2(d)]. (See Supplemental Material [48]). The retrieved spectra match remarkably well the theoretical results in Figs. 4(b) and 4(d).

## VI. LONG RANGE TEMPORAL DYNAMICS

Although our simulation scheme enables efficient mapping of the temporal edge bands (before $t < T_d' + \delta t_1$), it is also interesting to observe the temporal dynamics of edge modes and how to distinguish them from bulk modes in a practical measurement. In order to visualize the temporal localization of topological edge modes, we let the waves evolve for multiple repetitions of the temporal structure, and capture the scattering parameters at the beginning of every switching interval. In a first example, we implement the simulation of the temporal structure with parameters $(\theta_l, \beta_l)$ provided by the eigenvalue calculation such that we expect topological edge modes to be localized at the left temporal boundary of the temporal structure. The transmittance $|\gamma|^2$, with and without TCS next to the temporal supercell, are evaluated and shown in Fig. 5(a).

For the temporal structure with TCS, the period of the whole system is $T_d^{'} = T_{tqc} + T_{tcs}$, and $m = q + 1$ corresponds to the left boundary of TCS (marked by green line in Fig. 5). For the temporal structure without TCS, the period remains as $T_d = T_{tqc}$, so $m = q$ corresponds to the left boundary of the last temporal slab [marked by cyan line in Fig. 5(b)]. During the first instance of our temporal structure, as expected both transmitted waves $|\gamma|^2$ display the same patterns, until the switching event from temporal supercell to TCS occurs. After $t > T_{tqc}$, the waves in the first scenario propagate in the TCS with magnitude significantly reduced, because the permittivity $\varepsilon_{clad}$ is much larger than that in the temporal supercell. Interestingly, after the first temporal structure repetition, the waves demonstrate a drastically different response with or without TCS. After experiencing the TCS, the waves grow in amplitude during the first three switching intervals, and subsequently decay in a damped oscillatory pattern before the medium switches back to the temporal structure [red curve from theory and purple curve from FDTD in Fig. 5(a)]. This phenomenon verifies the appearance of the temporal edge modes during the second PTQC, consistent with the eigenvalue study in Fig. 3. By contrast, in the absence of TCS the wave grows exponentially in time after the first period of the temporal supercell, implying that no eigenstate exists in the momentum bandgap [blue curve from theory and cyan curve from FDTD in Fig. 5(a)].

In our second example, we choose the parameters $(\theta_b, \beta_b)$ corresponding to the temporal structure's bulk modes. Both scenarios with and without TCS show limited intensity, and display an oscillatory behavior in the time domain, confirming that bulk modes exist in both cases, as shown in Fig. 5(b). Next, we use the parameters $(\theta_r, \beta_r)$ corresponding to edge modes localized at the right temporal boundary. Similar to the first case, the temporal evolution of $|\gamma|^2$ with and without TCS is the same, and their dynamics become significantly different during the second period, see Fig. 5(c). For the temporal structure with TCS, the transmitted wave grows right after the switching event from temporal supercell to TCS. It then drops exponentially in the last three temporal slabs of the second temporal supercell, confirming the excitation of edge modes at the right boundary of the temporal structure. For the temporal structure without TCS, the excited wave constantly grows exponentially and behaves differently in the second period from the wave with TCS, which indicates the presence of momentum bandgap. Since $\varphi = \pi/2$, the period of the excited waves in these scenarios is equal to four times the driving period, thus the wave magnitude exhibits an oscillatory pattern double of the driving period, as shown in Fig. 5.

## VII. CONCLUSIONS

In this work, we have demonstrated the emergence of a Hofstadter butterfly spectrum and of a topologically nontrivial phase in temporal structures approximating PTQCs, and the occurrence of the temporal analog of topological edge states. We have also shown the transition dynamics of excited waves in synthetic space, establishing the temporal analog of topological pumping. Our work shows that temporally periodic and quasiperiodic structures like PTCs and PTQCs possess intriguing features not available in their spatial counterparts and offer opportunities for applications in various platforms, such as photonics, acoustics, and even in quantum systems of condensed matters [21]. Moreover, the numerical technique introduced in our work which efficiently solves the eigenvalue problems for photonic time (quasi)crystal and their topological properties, as well as closed-form relation between scattering coefficients and quasifrequency of the temporal structure, may give hints to the active research of a time (quasi)crystal. In particular, we note the extreme energy confinement of temporally evanescent waves occurring in the momentum bandgap of PTCs and PTQCs, which may be combined with nonlinear and non-Hermitian phenomena for other exotic wave phenomena. PTQCs may be realized both at radio frequencies with transmission-line metamaterials and in the optical regime exploiting all-optical pumping in polaritonic media [22,54–56].

## ACKNOWLEDGMENTS

This work was supported by the Science and Technology Center New Frontiers of Sound (NewFoS) through NSF Grant No. 2242925, the Air Force Office of Scientific Research MURI program and the Simons Foundation and the National Science Foundation. X.N. was partially supported by the Research Startup Funds of Central South University (Grant No. 11400–506030109) and the National Natural Science Foundation of China (Grants No. 12474396 and No. 12274240).

[1] F. Morgenthaler, Velocity modulation of electromagnetic waves, IRE Trans. Microw Theory Tech. **6**, 167 (1958).

[2] D. E. Holberg and K. S. Kunz, Parametric properties of fields in a slab of time-varying permittivity, IEEE Trans. Antennas Propag. **14**, 183 (1966).

[3] R. L. Fante, Transmission of electromagnetic waves into time-varying media, IEEE Trans. Antennas Propag. **19**, 417 (1971).

[4] H. Moussa, G. Y. Xu, S. X. Yin, E. Galiffi, Y. Ra'di, and A. Alu, Observation of temporal reflection and broadband frequency translation at photonic time interfaces, Nat. Phys. **19**, 863 (2023).

[5] P. K. Mukherjee and S. P. Talwar, Reflection and transmission of electromagnetic waves at a moving magnetoplasma half-space, Radio Sci. **8**, 653 (1973).

[6] A. Akbarzadeh, N. Chamanara, and C. Caloz, Inverse prism based on temporal discontinuity and spatial dispersion, Opt. Lett. **43**, 3297 (2018).

[7] E. Galiffi, P. A. Huidobro, and J. B. Pendry, Broadband nonreciprocal amplification in luminal metamaterials, Phys. Rev. Lett. **123**, 206101 (2019).

[8] H. Li and A. Alù, Temporal switching to extend the bandwidth of thin absorbers, Optica **8**, 24 (2021).

[9] V. Pacheco-Pena and N. Engheta, Temporal aiming, Light Sci. Appl. **9**, 129 (2020).

[10] Y. Mazor, M. Cotrufo, and A. Alù, Unitary excitation transfer between coupled cavities using temporal switching, Phys. Rev. Lett. **127**, 013902 (2021).

[11] H. Li, A. Mekaway, and A. Alù, Gain-free parity-time symmetry for evanescent fields, Phys. Rev. Lett. **127**, 014301 (2021).

[12] H. Li, S. X. Yin, E. Galiffi, and A. Alù, Temporal parity-time symmetry for extreme energy transformations, Phys. Rev. Lett. **127**, 153903 (2021).

[13] F. Biancalana, A. Amann, A. V. Uskov, and E. P. O'Reilly, Dynamics of light propagation in spatiotemporal dielectric structures, Phys. Rev. E **75**, 046607 (2007).

[14] J. R. Zurita-Sanchez, P. Halevi, and J. C. Cervantes-Gonzalez, Reflection and transmission of a wave incident on a slab with a time-periodic dielectric function, Phys. Rev. A **79**, 053821 (2009).

[15] J. R. Zurita-Sanchez, J. H. Abundis-Patino, and P. Halevi, Pulse propagation through a slab with time-periodic dielectric function, Opt. Express **20**, 5586 (2012).

[16] V. Pacheco-Pena and N. Engheta, Effective medium concept in temporal metamaterials, Nanophotonics **9**, 379 (2020).

[17] E. Yablonovitch, Accelerating reference frame for electromagnetic waves in a rapidly growing plasma: Unruh-Davies-Fulling-DeWitt radiation and the nonadiabatic Casimir effect, Phys. Rev. Lett. **62**, 1742 (1989).

[18] J. T. Mendonca, G. Brodin, and M. Marklund, Vacuum effects in a vibrating cavity: Time refraction, dynamical Casimir effect, and effective Unruh acceleration, Phys. Lett. A **372**, 5621 (2008).

[19] E. Yablonovitch, Inhibited spontaneous emission in solid-state physics and electronics, Phys. Rev. Lett. **58**, 2059 (1987).

[20] P. Lodahl, A. Floris Van Driel, I. S. Nikolaev, A. Irman, K. Overgaag, D. Vanmaekelbergh, and W. L. Vos, Controlling the dynamics of spontaneous emission from quantum dots by photonic crystals, Nature (London) **430**, 654 (2004).

[21] M. Lyubarov, Y. Lumer, A. Dikopoltsev, E. Lustig, Y. Sharabi, and M. Segev, Amplified emission and lasing in photonic time crystals, Science **377**, 425 (2022).

[22] H. Li, S. Yin, H. He, J. Xu, A. Alù, and B. Shapiro, Stationary charge radiation in anisotropic photonic time crystals, Phys. Rev. Lett. **130**, 093803 (2023).

[23] L. Lu, J. D. Joannopoulos, and M. Soljaclc, Topological photonics, Nat. Photon. **8**, 821 (2014).

[24] A. B. Khanikaev and G. Shvets, Two-dimensional topological photonics, Nat. Photon. **11**, 763 (2017).

[25] T. Ozawa H. M. Price, A. Amo, N. Goldman, M. Hafezi, L. Lu, M. C. Rechtsman, D. Schuster, J. Simon, O. Zilberberg, and I. Carusotto, Topological Photonics, Rev. Mod. Phys. **91**, 015006 (2019).

[26] Z. Wang, Y. D. Chong, J. D. Joannopoulos, and M. Soljacic, Observation of unidirectional backscattering-immune topological electromagnetic states, Nature (London) **461**, 772 (2009).

[27] Y. Poo, R. X. Wu, Z. F. Lin, Y. Yang, and C. T. Chan, Experimental realization of self-guiding unidirectional electromagnetic edge states, Phys. Rev. Lett. **106**, 093903 (2011).

[28] K. J. Fang, Z. F. Yu, and S. H. Fan, Realizing effective magnetic field for photons by controlling the phase of dynamic modulation, Nat. Photon. **6**, 782 (2012).

[29] M. C. Rechtsman, J. M. Zeuner, Y. Plotnik, Y. Lumer, D. Podolsky, F. Dreisow, S. Nolte, M. Segev, and A. Szameit, Photonic Floquet topological insulators, Nature (London) **496**, 196 (2013).

[30] M. Hafezi, S. Mittal, J. Fan, A. Migdall, and J. M. Taylor, Imaging topological edge states in silicon photonics, Nat. Photon. **7**, 1001 (2013).

[31] A. B. Khanikaev, S. H. Mousavi, W. K. Tse, M. Kargarian, A. H. MacDonald, and G. Shvets, Photonic topological insulators, Nat. Mater. **12**, 233 (2013).

[32] X. J. Cheng, C. Jouvaud, X. Ni, S. H. Mousavi, A. Z. Genack, and A. B. Khanikaev, Robust reconfigurable electromagnetic pathways within a photonic topological insulator, Nat. Mater. **15**, 542 (2016).

[33] A. Slobozhanyuk, S. H. Mousavi, X. Ni, D. Smirnova, Y. S. Kivshar, and A. B. Khanikaev, Three-dimensional all-dielectric photonic topological insulator, Nat. Photon. **11**, 130 (2017).

[34] B. Bahari, A. Ndao, F. Vallini, A. El Amili, Y. Fainman, and B. Kante, Nonreciprocal lasing in topological cavities of arbitrary geometries, Science **358**, 636 (2017).

[35] G. Harari, M. A. Bandres, Y. Lumer, M. C. Rechtsman, Y. D. Chong, M. Khajavikhan, D. N. Christodoulides, and M. Segev, Topological insulator laser: Theory, Science **359**, eaar4003 (2018).

[36] M. A. Bandres, S. Wittek, G. Harari, M. Parto, J. Ren, M. Segev, D. N. Christodoulides, and M. Khajavikhan, Topological insulator laser: Experiments, Science **359**, eaar4005 (2018).

[37] Y. E. Kraus, Y. Lahini, Z. Ringel, M. Verbin, and O. Zilberberg, Topological states and adiabatic pumping in quasicrystals, Phys. Rev. Lett. **109**, 106402 (2012).

[38] Y. E. Kraus and O. Zilberberg, Topological equivalence between the Fibonacci quasicrystal and the Harper model, Phys. Rev. Lett. **109**, 116404 (2012).

[39] M. Verbin, O. Zilberberg, Y. E. Kraus, Y. Lahini, and Y. Silberberg, Observation of topological phase transitions in photonic quasicrystals, Phys. Rev. Lett. **110**, 076403 (2013).

[40] E. Prodan, Virtual topological insulators with real quantized physics, Phys. Rev. B **91**, 245104 (2015).

[41] M. A. Bandres, M. C. Rechtsman, and M. Segev, Fractal topological spectrum and protected transport, Phys. Rev. X **6**, 011016 (2016).

[42] D. J. Apigo, W. Cheng, K. F. Dobiszewski, E. Prodan, and C. Prodan, Observation of topological edge modes in a quasiperiodic acoustic waveguide, Phys. Rev. Lett. **122**, 095501 (2019).

[43] X. Ni, K. Chen, M. Weiner, D. J. Apigo, C. Prodan, A. Alu, E. Prodan, and A. B. Khanikaev, Observation of Hofstadter butterfly and topological edge states in reconfigurable quasi-periodic acoustic crystals, Commun. Phys. **2**, 55 (2019).

[44] E. Lustig, Y. Sharabi, and M. Segev, Topological aspects of photonic time crystals, Optica **5**, 1390 (2018).

[45] M. Oudich, Y. C. Deng, M. L. Tao, and Y. Jing, Space-time phononic crystals with anomalous topological edge states, Phys. Rev. Res. **1**, 033069 (2019).

[46] Y. Sharabi, E. Lustig, and M. Segev, Disordered photonic time crystals, Phys. Rev. Lett. **126**, 163902 (2021).

[47] R. Carminati, H. Chen, R. Pierrat, and B. Shapiro, Universal statistics of waves in a random time-varying medium, Phys. Rev. Lett. **127**, 094101 (2021).

[48] See Supplemental Material at http://link.aps.org/supplemental/10.1103/PhysRevB.111.125421 for the derivation of conventional eigenvalue equation, several proofs of the properties of our temporal structure, the details of FDTD simulations, connections between PTQCS and Aubry-Andrè model and FDTD simulations for the Hofstadter butterfly spectrum, which includes Refs. [49–51].

[49] J. E. Avron, D. Osadchy, and R. Seller, Topological quantum numbers in the Hall effect, Phys. Today **56**, 38 (2003).

[50] *Theory and Computation of Electromagnetic Field*, edited by J. M. Jin (Wiley, New York, 2010).

[51] F. Liu, S. Ghosh, and Y. D. Chong, Localization and adiabatic pumping in a generalized Aubry-André-Harper model, Phys. Rev. B **91**, 014108 (2015).

[52] P. G. Harper, Single band motion of conduction electrons in a uniform magnetic field, Proc. Phys. Soc. London A **68**, 874 (1955).

[53] S. Aubry and G. Andre, Analyticity breaking and Anderson localization in incommensurate lattices, Ann. Isr. Phys. Soc. **3**, 18 (1980).

[54] J. R. Reyes-Ayona and P. Halevi, Observation of genuine wave vector (k or $\beta$) gap in a dynamic transmission line and temporal photonic crystals, Appl. Phys. Lett. **107**, 074101 (2015).

[55] Y. Y. Zhou, M. Z. Alam, M. Karimi, J. Upham, O. Reshef, C. Liu, A. E. Willner, and R. W. Boyd, Broadband frequency translation through time refraction in an epsilon-near-zero material, Nat. Commun. **11**, 2180 (2020).

[56] V. Bruno, C. DeVault, S. Vezzoli, Z. Kudyshev, T. Huq, S. Mignuzzi, A. Jacassi, S. Saha, Y. D. Shah, S. A. Maier, D. R. S. Cumming, A. Boltasseva, M. Ferrera, M. Clerici, D. Faccio, R. Sapienza, and V. M. Shalaev, Negative refraction in time-varying strongly coupled plasmonic-antenna–epsilon-near-zero systems, Phys. Rev. Lett. **124**, 043902 (2020).